Scientific Research Publishing

Open Journal of Fluid Dynamics, 2024, 14, 163-183
https://www.scirp.org/journal/ojfd
ISSN Online: 2165-3860
ISSN Print: 2165-3852

Channel Flows in Plate Heat Exchangers with the Aid of Particle Tracking Velocimetry

Felipe José dos Santos[1], Leonel Edward Beckedorff[2], Kleber Vieira de Paiva[3], Jorge Luiz Goes Oliveira[3]

[1]PETROBRAS—Petróleo Brasileiro S.A., Rio de Janeiro, Brazil
[2]Institute of Fluid Mechanics and Heat Transfer, Technische Universität Wien, Vienna, Austria
[3]Department of Mobility Engineering, Federal University of Santa Catarina, Joinville, Brazil
Email: felipezurus@gmail.com, leonelbeckedorff@gmail.com, kleber.paiva@t2f.ufsc.br, jorge.goes@t2f.ufsc.br

How to cite this paper: dos Santos, F.J., Beckedorff, L.E., de Paiva, K.V. and Oliveira, J.L.G. (2024) Channel Flows in Plate Heat Exchangers with the Aid of Particle Tracking Velocimetry. *Open Journal of Fluid Dynamics*, **14**, 163-183.
https://doi.org/10.4236/ojfd.2024.143008

Received: May 20, 2024
Accepted: September 9, 2024
Published: September 12, 2024

Abstract

Channel flows of Plate Heat Exchangers (PHEs) were assessed by experiments with three different chevron angle arrangements in turbulent regime. Two chevron angles were selected to assess low and high pressure drop channels, besides a third mixed configuration as to achieve in-between results regarding hydraulic performance. Friction factor correlations were provided with the channel Reynolds number ranging from 1175 to 8325. Two-dimensional (2D) mean velocity field was obtained by Particle Tracking Velocimetry (PTV) with Reynolds number equal to 3450. To the best of our knowledge, this is the first experimental study that quantified the complete 2D velocity field of a typical PHE channel. This value allowed comparison with literature results of Plate and Shell Heat Exchanger (PSHE) channels with the same Reynolds number. PSHE mean velocity field is highly heterogeneous as compared to the one obtained for PHE channels. Peak velocity magnitude in the PSHE center is 50% higher than its bulk velocity, whereas this value is only 15% higher in the PHE center. Pressure drop in PHE mixed channels cannot be approximated by averaging chevron angles: furrow flow prevailed in the specified conditions. The axial velocity is asymmetric regarding the vertical plane. Smooth streamlines prevail in the channel inlet. Recirculation zones at the channel exit affect pipe flow in the manifold outlet with swirling flow structures. The necessary length to obtain fully developed pipe flow at the channel outlet was estimated. Significant velocity components occur in the distribution areas and can limit the heat exchanger performance. The results reported herein are essential to understand how the PHE channel geometry affects the velocity field and, therefore, local heat transfer and dissipation processes.

Keywords

PHE, PTV, PSHE, Friction Factor, Chevron

1. Introduction

Plate Heat Exchangers (PHE) are widely used in many industries such as refrigeration, oil production, power generation, chemical and food processing. These exchangers provide high heat transfer coefficients, reduced fouling, and are relatively compact. A typical gasketed plate heat exchanger consists of a stack of rectangular thin plates with wavy surfaces held together in a frame by compression bolts, Kakaç *et al.* [1]. Flow channels are sealed by gaskets, which prevent leaking and intermixing of the fluid streams. Plate heat exchangers allow operations with a maximum pressure of about 30 bars and temperature levels up to 260˚C, Shah and Sekulic [2].

Several works were carried out to investigate the performance of PHEs with chevron plates. Single-phase flow correlations for heat transfer and friction factor coefficients were provided by numerous authors; see references [3]-[10], for example. Detailed literature reviews on corrugated plate heat exchanger and heat transfer enhancement techniques in PHEs were presented by Elmaaty *et al.* [11] and Zhang *et al.* [12], and more recently by Arsenyeva *et al.* [13]. It is consensual that the chevron angle is the most influential geometrical parameter in PHE design.

Experimental studies with visualization techniques were conducted by Focke *et al.* [14] and Dović and Svaic [15]. Differently from previous studies [3]-[10], which are essentially based on averaged quantities, the latter visualization investigations [14] [15] allow appraisal of local flow features. Fluid particle trajectory patterns were addressed for different chevron plate configurations, for example. For chevron angles less than 45˚ (angle between the corrugated channels and the vertical edge of the plate) fluid flows mainly along the furrows, whereas, for higher angles, wavy longitudinal flow is predominant. Martin [16] considered the combined effects of each flow pattern in PHE channels to derive an equation for the friction factor as a function of the corrugation angle and the Reynolds number. Heat transfer coefficients were also obtained for turbulent channel flows. Attempts to provide precise and generalized PHE correlations, which include the correlation dependence on Reynolds numbers, chevron angles and corrugation aspect ratios, have been proposed by Arsenyeva *et al.* [17]-[19].

Despite the extensive research on PHE design parameters, few studies had investigated the velocity field within PHE channels. To the best of our knowledge, this is the first experimental study that quantified the complete 2D velocity field of a typical PHE channel. Previous investigations are restricted to an averaged cross-section velocity at the PHE heat transfer area [3]-[10] [16]-[19], or to qualitative fluid particle trajectory descriptions [14] [15]. The present results are

essential to understand how the PHE channel geometry affects the velocity field and, therefore, local heat transfer and dissipation processes. The results reported herein are crucial to understand why correlations of friction factors and Nusselt numbers obtained in the literature yield significant differences in GPHE design; see Santos *et al.* [20].

In this study, the effect of the PHE plate geometry on the 2D mean velocity field of typical channels will be investigated with the aid of Particle Tracking Velocimetry (PTV). Assessment occurs with narrow acrylic sheets, machined to match the PHE channel geometry and ensure visual accessibility. Three different chevron angle arrangements (30˚/30˚, 60˚/60˚ and 30˚/60˚) were applied in turbulent flow regime. The first and second arrangements are representative of low and high pressure drop channels, respectively, while the third configuration is an attempt to achieve in-between results regarding hydraulic performance. Friction factor correlations will be provided for water flows with the Reynolds number, based on the PHE hydraulic diameter, ranging from 1175 to 8325.

PTV measurements occurred with Reynolds number equal to 3450. This value was selected as to allow comparison with the velocity field of Plate and Shell Heat Exchanger (PSHE) channels measured with PTV by Beckedorff *et al.* [21] [22] with the same Reynolds number and with chevron angle arrangement of 45˚/45˚. As a consequence, the effect of rectangular or circular corrugated plate geometries on the mean velocity field can be compared. Additionally, the effect of the flow behavior at the channel outlet on the exit pipe flow has been examined. The decay of swirling flow structures and the necessary length to obtain fully developed pipe flow were estimated with the aid of literature results.

2. Methodology

2.1. Test Rig

Figure 1 presents the experimental setup used to investigate PHE channel flows. Siemens Sinamics V20 controlled centrifugal pumps (Multisteel, type RF 32/160) as to fine-tuning of the Reynolds number in the measurement section. Mass flow rate is measured employing a Rosemount 8700M magnetic flowmeter (inaccuracy is less than 0.5% of the registered flow rate). A mesh flow conditioner is placed 40 pipe diameters upstream of the test section. Following Laws *et al.* [23], a nearly developed flow at the PHE channel entrance is expected. The flow is then conducted back to the water reservoir.

Omega transducers, type PX409 (0.08%FS uncertainty), allowed absolute and differential pressure measurements (not shown in Figure 1). The absolute pressure is monitored at the test section entrance by Omega transducers with the aid of pressure taps. Omega 100Ω platinum RTD monitors water temperature in the flow loop. National Instruments acquisition systems were applied to collect measuring data, monitored through LabVIEW software. Downward and upward flows have been tested to confirm that gravity would not affect adiabatic flows within PHE channels. Table 1 summarizes sensors' uncertainty specification.

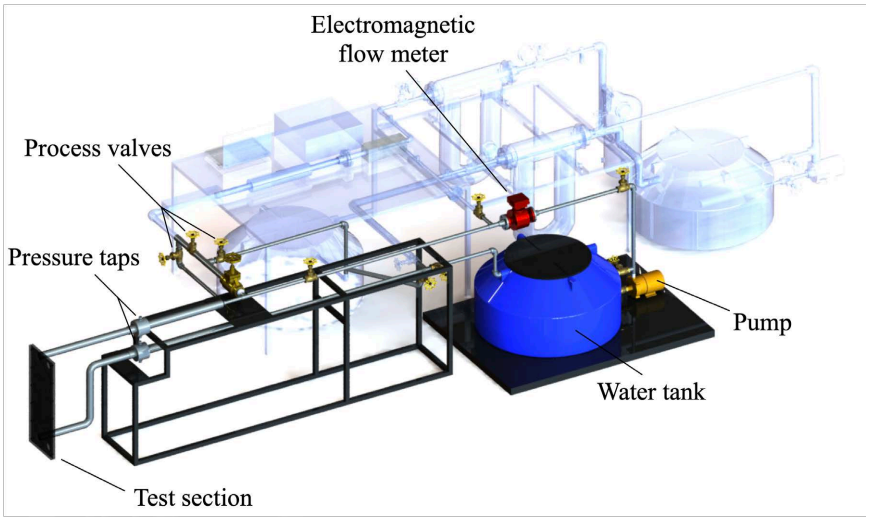

Figure 1. Multiphase flow experimental setup schematics. Only the water circuit (colorful graphic) was applied for experiments.

Table 1. Uncertainty specification of applied sensors.

Parameter	Specification	Uncertainty
Water flow meter	Rosemount 8700M magnetic flowmeter	0.5 (%RD)
Absolute pressure transducer	Omega PX409 (absolute)	0.08 (%FS)
Differential pressure transducer	Omega PX409 (differential)	0.08 (%FS)
Temperature sensor	RTD PT100-PMA-1/8-6-1/8-R-3	(0.15 + 0.002T)˚C

Water flows were measured within PHE channels by Particle Tracking Velocimetry (PTV) with a fast camera (SpeedSense type). It has 12-bit grayscale CMOS sensor and a resolution of 1280 × 1280 pixels. Nikon 18 - 200 mm f/3.5 - 5.6 lens was used to capture almost instantaneous particle positions in a 211 × 695 mm^2 rectangular area of the test section. The camera operated at 1000 Hz. The experimental settings can be summarized as: pixel sensor resolution equal to 10 μm^2; focal length of 100 mm; exposure time of 1 ms; distance from the lens to the object of 0.95 m. In order to reduce reflections to the fast camera, a lighting system consisting of LEDs was positioned around the channel.

2.2. Test Sections

Two pairs of acrylic sheets with the thickness equal to one inch were machined to generate PHE channels. Each pair of sheets was machined with different corrugation angles. Several bolts press a pair of sheets against each other and a gasket which circumvents them as to assure ideal sealing. The primary dimensions of the frontal view of a single plate which composes the PHE channel are presented in **Figure 2(a)**. The origin of the Cartesian coordinate system is at the frontal view center. Gravity is antiparallel to the y-axis. The variable β stands for chevron angle: the angle formed by the corrugation and the y-axis. The chevron

angle is well-known to affect thermal and hydraulic behaviors of GPHEs as showed in the study of Yang, Jacobi and Liu [9], who presented increasing heat transfer and friction factor coefficients with increasing β-values.

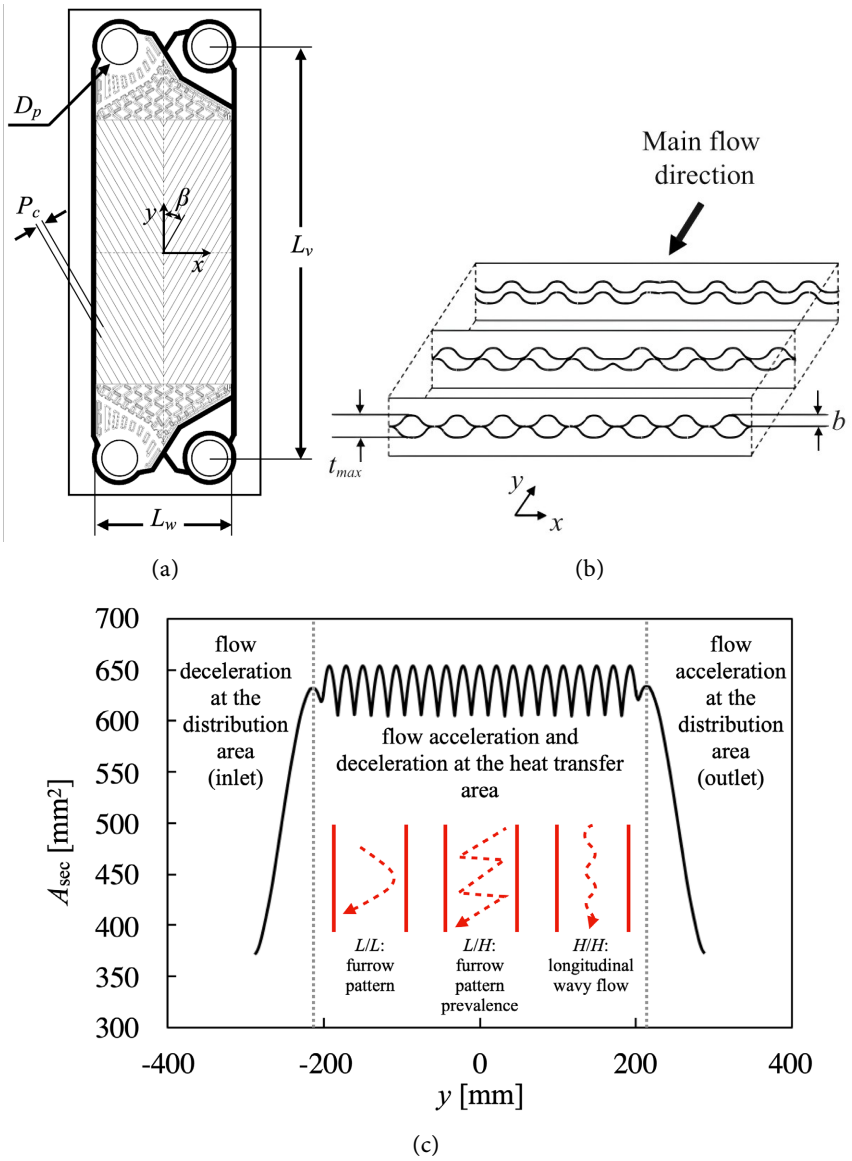

Figure 2. Test section features of PHE channels: (a) frontal view main dimensions for one plate, (b) cross-section complex form and (c) cross-section variation along the axial direction (y-axis).

With the motivation of investigating PHE hydraulic features affected by different β-values, three chevron arrangements were tested: 30˚/30˚, 30˚/60˚ and 60˚/60˚. The acrylic sheets were built in a way that allowed the use of different corrugation angles to form a channel. 30˚/30˚ configuration typifies channels with a minimal pressure decrease (*i.e.* L-channels), whereas 60˚/60˚ arrangement characterizes channels with substantial pressure drop (*i.e.* H-channels). Following the flow pattern chart of Sarraf *et al.* [24] and for channel Reynolds numbers

surpassing 500, furrow or spiral flow patterns manifest in L-channels, whereas longitudinal wavy or cross-flow patterns arise in H-channels. Flows in PHE channels encompass both configurations with 30˚/60˚ arrangement, with a prevalence of the furrow pattern under the specified boundary conditions.

Cross-section complex form is shown with the aid of Figure 2(b): note the presence of several irregular areas along the y-axis. Cross-section values along y-axis, denoted as Asec, are presented in Figure 2(c) in a line segment which comprises the channel inlet and outlet centers; see the variable L_v in Figure 2(a). Dissipation processes are very intense in the inlet and outlet distribution zones: $y < -200$ mm and $y > 200$ mm in Figure 2(c). Flow experiences deceleration and acceleration with high velocity components. Within the heat transfer zone, the periodic cross-section variation encompasses components of low fluid velocity. Channel primary geometric characteristics are summarized in Table 2.

Table 2. Channel primary geometric characteristics.

Parameter	Symbol	Value
Chevron angle (˚)	β	30/30, 30/60, 60/60
Length between the inlet and outlet centers (mm)	L_v	639
Plate width (mm)	L_w	211
Port diameter (mm)	D_{port}	56
Corrugation depth (mm)	b	3
Corrugation pitch (mm)	P_c	10.75
Enlargement factor (-)	ϕ	1.17
Hydraulic diameter (mm)	D_h	5.14

2.3. PTV Method—Applied Particles and PTV Algorithm

Gravel seeding particles were added to the water as flow tracers. To assure these particles could represent main flow structures, time and length scales of particles and fluid were compared as well as the effect of gravity on particles, and the effect of fluid acceleration on particle motion. The incorporation of these particles into the water has been a consistent practice in our prior studies, as documented by Beckedorff *et al.* [21] [22].

Following Albrecht *et al.* [25], relaxation time for particles, τ_p, in stationary flow is given by:

$$\tau_p = \left(d_p{}^2 \rho_p / 18\mu\right)\left(1 + 0.5\rho_f / \rho_p\right) \quad (1)$$

where d_p is the particle diameter, ρ is the mass density and μ is the dynamic viscosity. The subscripts p and f stand for particle and fluid, in that order. The relaxation time of the gravel particle with a diameter of 0.15 mm is 2.6 ms. Prior values are then compared to dissipative fluid time and length scales. By applying viscous wall units and adopting Kolmorogov scales as the fluid ones, one finds $\tau_k = \nu / u_\tau^2$ and $l_k = \nu / u_\tau$, respectively, where ν is the kinematic viscosity and u_τ,

the wall shear velocity. The latter is defined as $u_\tau = (\tau_w/\rho_f)^{1/2}$ where τ_w is the wall shear stress. An approximation of the magnitude order can be achieved by utilizing $\tau_w = \mu v_B/t_{ave}$,, where t_{ave} is the average channel height and equals to 3 mm, and v_B is the bulk velocity at the PHE center (plane $y = 0$). For $v_B = 605$ mm·s^{-1}, the estimated values for τ_w, u_τ, l_k, and τ_k are as follows: 0.20 Pa, 14.23 mm·s^{-1}, 0.0705 mm, and 4.9 ms, respectively. Time- and length-scale ratios for particles and fluid are now presented with the Stokes number, $\mathrm{St} = \tau_p/\tau_k \approx 0.5$, and with the ratio $d_p/l_k \approx 2$. It is concluded that the main flow scales can be captured by applied gravel particles.

In addition, the effect of gravity on particles can be measured by comparing the final velocity of the gravel particles with the bulk flow velocity, while the effect of fluid acceleration on particle motion can be demonstrated by comparing the ratio of pressure gradient forces (including additional mass forces) to buoyancy forces. For actual boundary conditions, both effects are negligible, see references [21] [22].

The methodology for identifying separate particle trajectories through PTV resembles the approaches employed by Oliveira *et al.* [26]-[28] in pipe flow and Beckedorff *et al.* [21] [22] in a PSHE channel. Tracer trajectories were acquired with the aid of Davis PTV code from La Vision. References [29] [30] provided detailed information on the algorithm used for tracking. Processing calibration images establish a correlation between pixel data and the physical dimensions of the calibration plate. The latter is made of plastic, 0.5 mm thick, and it contains circular voids regularly spaced in 20 mm in both horizontal and vertical dimensions. The plate surface area has been cut to match the xy-plane flow area of **Figure 2(a)**, *i.e.* the projection of the frontal view area where PHE channel flow occurs. A third-order polynomial establishes a correlation between pixel data and physical dimensions of the calibration plate, achieving an RMS error of less than 0.5 pixels, or approximately 5 μm. Once the calibration procedure is completed, flow measurement images generate files containing the time and space positions of separate particle trajectories.

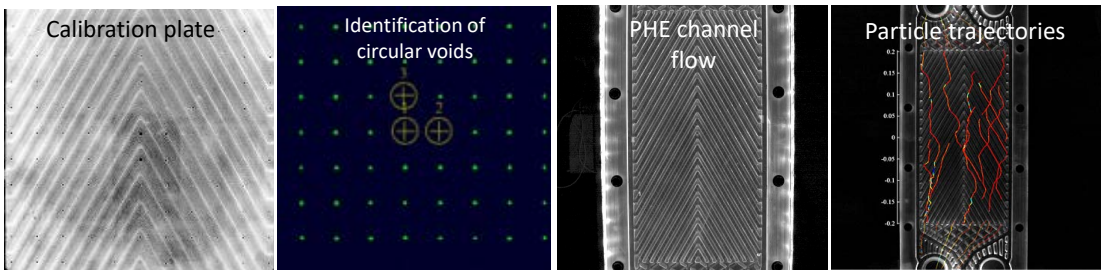

Figure 3. Photographs of the PTV method: (a) calibration plate image at the channel center, (b) identified voids (in green), (c) channel flow image, and (d) integration of separate tracer trajectories within a limited time span.

Figure 3 shows photographs of the PTV method. **Figure 3(a)** displays calibration plate image at the channel center, while **Figure 3(b)** illustrates the identified

voids (in green). Note that the calibration recording is registered at a single position, limiting the trajectory analysis to the channel frontal view plane. Figure 3(c) shows channel flow image: note that light noise is significant. Imaging filters enhance the contrast between the object and the background as to facilitate identification of particle tracks. Particles centers' are identified with the aid of a Gaussian fit. Space and time references of each particle identified are exported to the analysis method; see the integration of individual tracer trajectories within a limited time window in Figure 3(d).

2.4. Trajectory Analysis Method

Figure 4 shows the applied PTV mesh. Figure 4(a) shows separate bins projected on the channel frontal view (left), and geometry of a measurement bin (right). Figure 4(b) shows discrete bins projected in the frontal view of the channel inlet or outlet (left), and geometry of a measurement bin at the same positions (right). False trajectories generated during the PTV procedure are discarded by a length filter and a displacement outlier-check at the channel periphery [21] [22]. False trajectories were mostly created by light reflections at the channel edges. Afterwards, velocity vectors in the plane of view are attained by the differentiation of the validated trajectories with regard to time. Over 100,000 velocity vectors were obtained with twenty individual measurement sets of 2 s. Finally, ensemble-averaging of velocity vectors at grid points around of Figure 4 is performed.

The grid volume at the center of the channel is 3217 mm^3, and at the inlet/outlet, 533 mm^3. PTV measurements were obtained with the Reynolds number, based on the PHE hydraulic diameter, equal to 3,450. A camera frequency of 1000 Hz was applied. Flow measurement analysis at the channel inlet and outlet undergo conversion from Cartesian to cylindrical coordinates, with the origin at the center of the inlet and outlet manifolds. Radial velocities, denoted as vrad, are collected in bins of Figure 4(b).

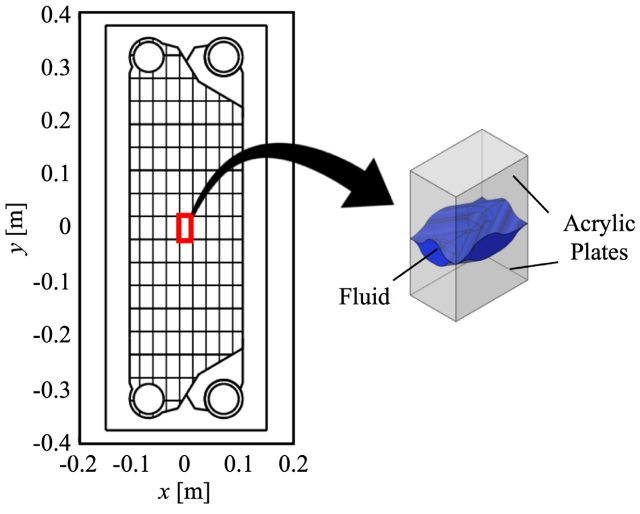

(a)

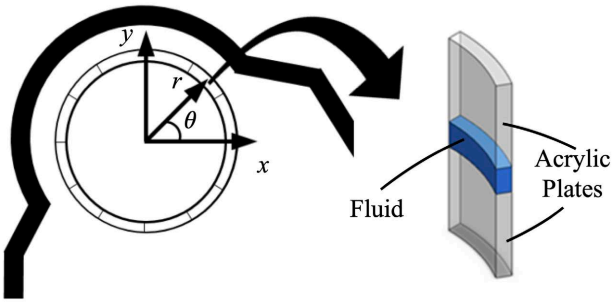

(b)

Figure 4. Discrete bins projected on the channel frontal view ("a"—left) and geometry of a measurement bin ("a"—right). Discrete bins projected in the frontal view of the channel inlet or outlet ("b"—left) and geometry of a measurement bin at the same positions ("b"—right).

Method validation occurred with mass flow rate integration in different channel cross-sections. Integration was obtained with the product of the mean axial velocity and the cross-sectional area of each grid. With the mass density of water at nearly atmospheric condition, one can find the PTV mass flow rate in different y-planes. Finally, PTV accuracy was guaranteed by comparisons with the electromagnetic flowmeter reading at 15 cross-sections. These results match within experimental error.

2.5. Determination of Friction Factors

To calculate the frictional pressure drop (ΔP_{ch}), it was adopted a procedure similar to that employed by references [20] [31]. Needles were positioned at the channel entry and exit by creating small holes through the gasket sealing. Friction factor can be calculated according to:

$$f = \frac{2\Delta P_{ch} D_h \rho}{4L_v \left(\frac{\dot{m}_{ch}}{A_{\text{sec}}} \right)^2} \tag{2}$$

$$D_h = \frac{2b}{\phi} \tag{3}$$

where $\dot{m}_{ch}$ denotes the channel mass flow rate, and D_h is the hydraulic diameter. The variable ϕ represents the enlargement factor, defined as the ratio of the effective to the projected plate area [1]. Following the approach of reference [16], ϕ can be computed as:

$$\phi = 1/6\left(1+\sqrt{1+x^2}+4\sqrt{1+x^2/2}\right) \tag{4}$$

where x represents the corrugation number, $\pi b/P_c$. Following Beckedorff *et al.* [32], the maximum uncertainty for friction factors was ±5.5%, calculated in accordance with:

$$u(f) = \left(\frac{\rho D_h \Delta P A_{ch}^2}{2DL_v \dot{m}_{ch}^2} \right) \left\{ \left(\frac{u(\Delta P)}{\Delta P} \right)^2 + \left(-2\frac{u(\dot{m}_{ch})}{\dot{m}_{ch}} \right)^2 \right\}^{0.5} \tag{5}$$

3. Results

3.1. PHE Channel Flow

Figure 5(a) shows the effect of chevron angle arrangements (30˚/30˚, 30˚/60˚ and 60˚/60˚) on the channel pressure drop (ΔP_{ch}) and Figure 5(b), on the Fanning friction factor. Circles, diamonds and triangles represent L/L, L/H and H/H arrangements, in that order. The Reynolds numbers, Re, based on the cross-section area, Asec, ranged approximately from 1175 to 8325:

$$\mathrm{Re} = \frac{m_{ch} D_h}{A_{\mathrm{sec}} \mu} \tag{6}$$

Kakaç *et al.* [1] defined flow regime as turbulent for channel Reynolds numbers over 400. The same flow regime is considered according to Bond [33] and Gusew and Stuke [34].

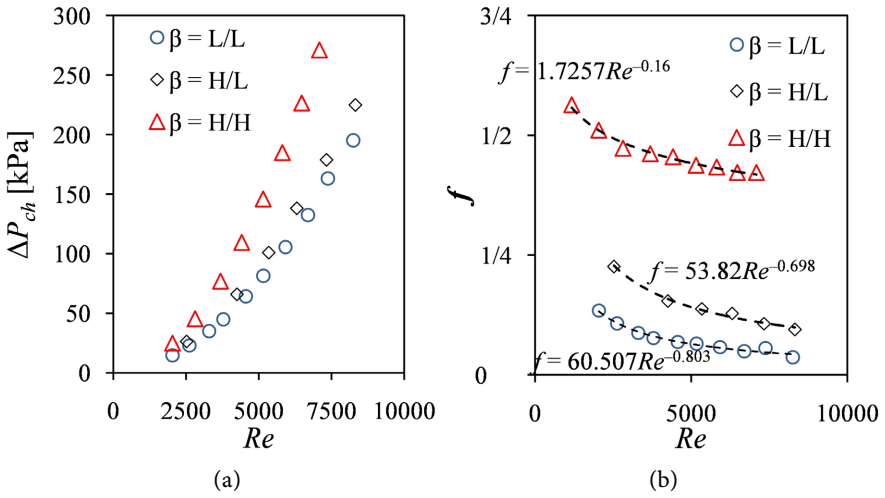

Figure 5. Effect of chevron angle arrangement on PHE pressure drop (a) and on the friction factor (b). Circles, diamonds and triangles represent L/L, L/H and H/H arrangements, in that order.

For the same Reynolds number, channel pressure drop increases with increasing chevron angles owing to the increased flow disturbance in longitudinal wavy flows as compared to furrow patterns; see Sarraf *et al.* [24], for example. Note that the pressure drop in mixed channels cannot be approximated by averaging the chevron angle arrangement: it is slightly higher than the one presented for L-channels. Despite the occurrence in mixed channels of both patterns (furrow and longitudinal wavy), furrow pattern prevails in the present conditions.

Table 3 summarizes friction factor correlations for the actual experiments. R^2-values over 0.98 assure the quality of each fit.

Figure 6 shows the mean axial (a) and lateral (b) velocity components for chevron angle arrangements of 30˚/30˚, and with channel Reynolds number equal to 3450. Despite the differences in fluid particle trajectories with respect to the channel chevron angle, the projection of the mean velocity components onto

the channel frontal view is comparable. Therefore, for the sake of brevity, results were only presented for one chevron angle configuration. With the aim of comparing the effect of rectangular and circular corrugated plate geometries on the mean velocity field, Figure 6 also presents the mean axial (c) and lateral (d) velocity components for a Plate and Shell Heat Exchanger (PSHE) channel with the same Reynolds number and with chevron angle arrangements of 45˚/45˚, as investigated by Beckedorff *et al.* [22]. The PSHE plate external diameter is 295 mm, and its heat transfer area is nearly half of the PHE area.

Table 3. PHE friction factor correlations obtained with water flows. Prandtl number is 4.3, and the Reynolds number is in the range 1175 - 8325.

Chevron angles	Correlations
30˚/30˚	$f = 60.507 Re^{-0.803}$
30˚/60˚	$f = 53.82 Re^{-0.698}$
60˚/60˚	$f = 1.7257 Re^{-0.16}$

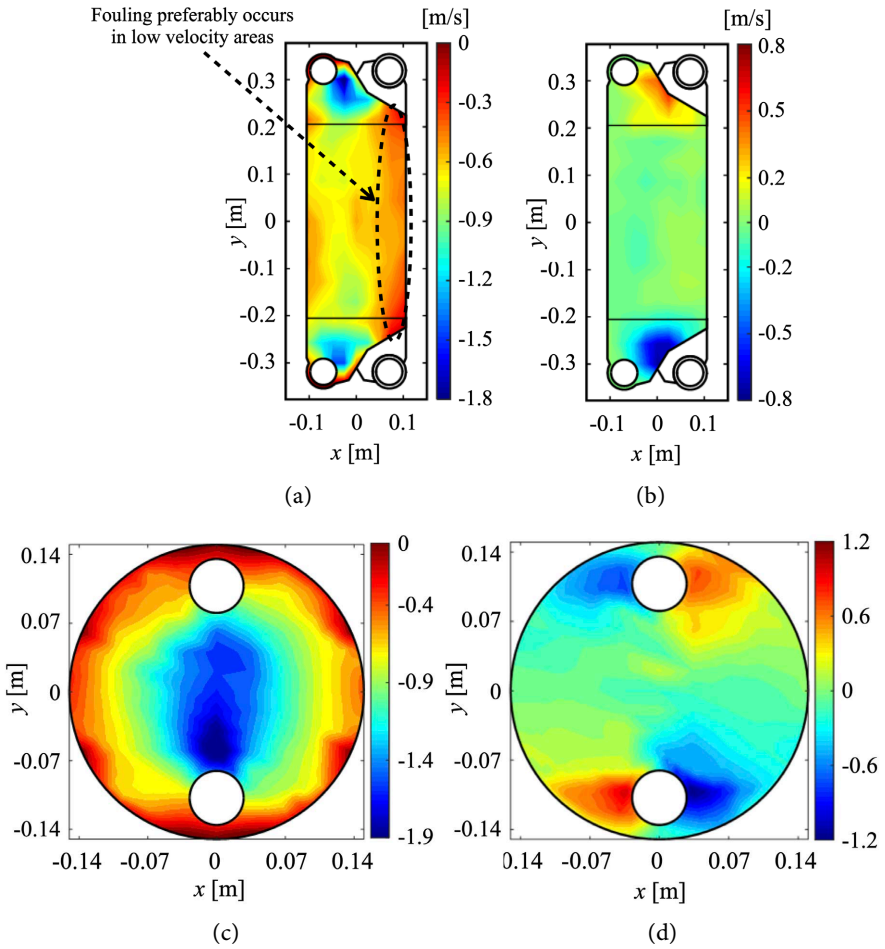

Figure 6. Effect of the corrugated channel geometry on the mean velocity field: (a) axial (PHE), (b) lateral (PHE), (c) axial (PSHE) and (d) lateral (PSHE) components. Downward flows were measured. PHE and PSHE chevron angle arrangements are 30˚/30˚ and 45˚/45˚, respectively.

The asymmetry in the mean axial velocity concerning the plane $x = 0$ is evident in Figure 6(a). In the left region of the channel (-0.2 m $< y <$ 0.2 m; $x < 0$), the flow resistance is reduced due to the shorter exit length: note that yellow color indicates velocities with higher magnitude in regard to orange/red colors. Fouling preferably occurs in low-velocity areas (-0.2 m $< y <$ 0.2 m; $x >$ 0.05; see dashed line in Figure 6(a). The distribution regions exhibit the highest axial velocities ($y < -0.2$ m; $y >$ 0.2 m) due to mass conservation, as seen in the blue regions of Figure 6(a). The lateral bulk approaches zero in the central region (-0.2 m $< y <$ 0.2 m), as illustrated in Figure 6(b). Lateral velocity is nearly anti-symmetric concerning the plane $y = 0$; compare yellow/red colors for $y >$ 0.2 m to light and dark blue areas for $y < -0.2$ m.

Comparison of Figures 6a and 6c reveals that the PHE mean velocity field is more homogenous in the heat transfer area in regard to the PSHE velocity field. Average axial velocity components are meaningful in the PSHE central area (-0.08 m $< y <$ 0.08 m; -0.05 m $< x <$ 0.05 m), see light and dark blue colors in Figure 6(c). The short distance between ports promotes high velocities. Fouling preferably occurs near the external circumference in the PSHE channel, where axial bulk velocities approach zero. The peak velocity magnitude in the PSHE center point ($y = 0$; $x = 0$) is 1.5 v_B, whereas this value is 1.15 v_B in the PHE center point. Figure 6(d) reveals that the lateral velocity is nearly anti-symmetric concerning planes $y = 0$ and $x = 0$. Maximum lateral velocity is nearly 0.45 v_B for the PHE channel, and roughly 0.63 v_B for the PSHE channel.

Figure 7(a) and Figure 7(b) present profiles of the mean axial and lateral velocity components, in that order, in five PHE y-positions: three in the heat transfer area (-0.13, 0 and 0.13) and two in the distribution regions (-0.26 and 0.26); see Figure 7(c). The velocity is made non-dimensional with the bulk velocity, v_B, at the PHE center ($y = 0$).

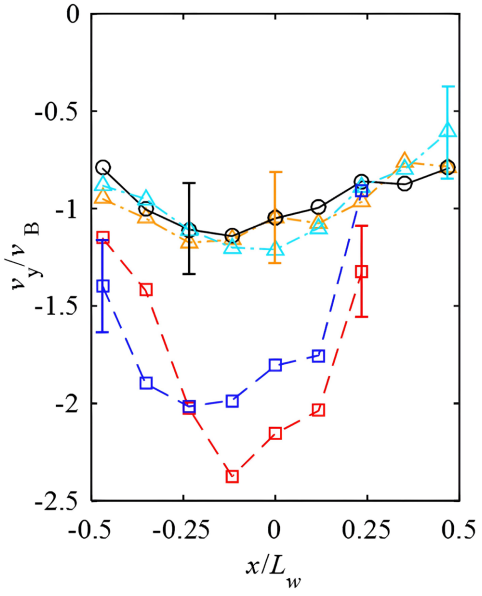

(a)

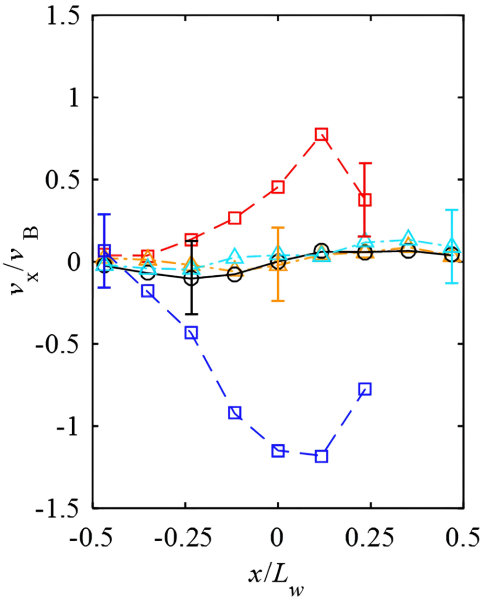

(b)

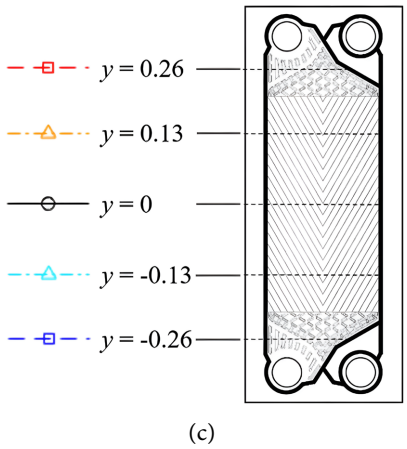

(c)

Figure 7. Effect of the PHE channel geometry on the mean velocity: (a) axial and (b) lateral components in five y-positions (c). Downward flows were measured.

The asymmetry of the mean axial velocity field is demonstrated with the aid of **Figure 7(a)**. At the channel mid-plane, the peak axial velocity is 1.15 v_B and occurs at $x/Lw = -0.11$, whereas the relative horizontal velocity is nearly zero. At the distribution regions, plane $y = \pm 0.26$, the maximum velocity reaches 2.4 v_B at the entrance, and 2 v_B at the exit. Error-bars (standard errors with confidence intervals of 95%) give an indication of the variation of velocity over the channel height. Note that the magnitude of the lateral velocity is higher at the outlet distribution, **Figure 7(b)**. Significant velocity components in the distribution areas (as shown in planes $y = \pm 0.26$) will play important role in the PHE dissipation process. In accordance to reference [13], the pressure drops at the channel inlet and outlet with the distribution zones can account for up to 50% of the total pressure drop in the PHE.

Figure 8(a) shows the dimensionless mean radial velocities at the inlet and

exit ports. Cylindrical coordinate systems with their origins at the ports' centers are used, as indicated in the top/left of Figure 8(a) and in Figure 4(b). Outlet and inlet results are plotted in clockwise and in counter clockwise directions, in that order. Figure 8(b) shows linear streamlines in radial direction at the channel inlet with the join of separate tracer trajectories in a limited time span, while Figure 8(c) highlights the recirculation zones formed at the channel outlet with the aid of air bubbles added to the main stream.

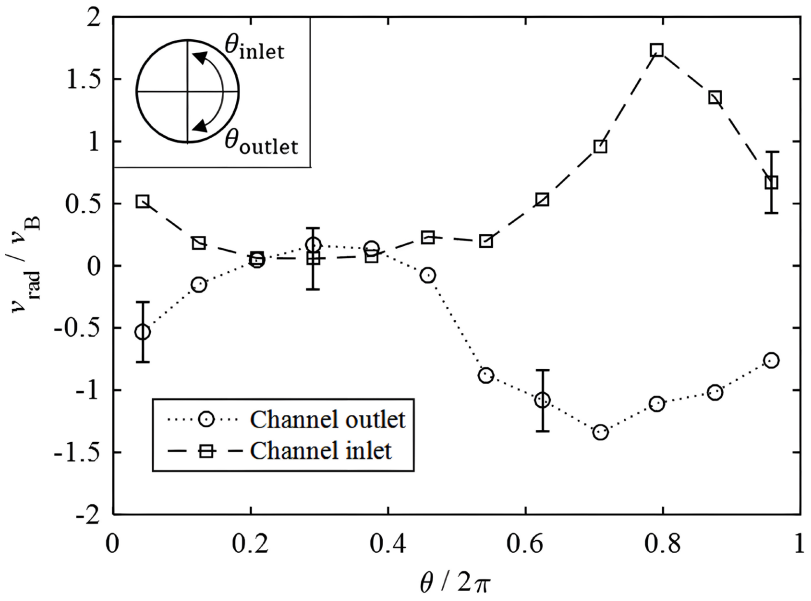

(a)

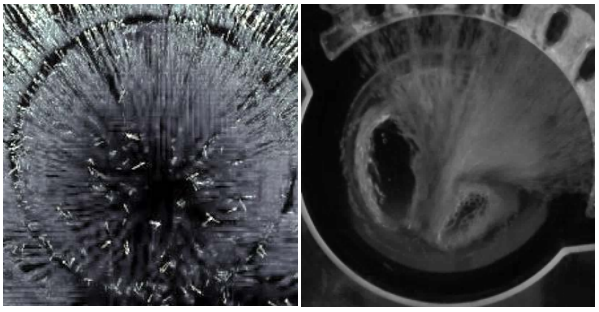

(b) (c)

Figure 8. Dimensionless mean radial velocities at the inlet and exit ports (a); linear streamlines in radial direction at the channel inlet (b); recirculation zones at the channel outlet (c).

The radial velocity can reach up to 1.4 v_B at the PHE exit, and it can exceed 1.7 v_B at the entrance. The PHE channel outlet exhibits flow recirculation (Figure 8(c)), influencing the radial velocity distribution. The annular cross-section surrounding the PHE channel outlet is smaller than the exit pipe cross-section, resulting in flow deceleration and increased static pressure. This pressure rise induces boundary layer separation near the channel outlet, leading to the formation of recirculation zones. Similar behavior was found at the exit of PSHE

channel by reference [21]. On the fictional closed curves, the average measured fluid velocity is 0.7 $m \cdot s^{-1}$. Conversely, at the channel inlet, the flow accelerates while static pressure decreases, allowing flow trajectories to enter the PHE channel along roughly linear streamlines in radial direction (Figure 8(b)).

3.2. Manifold Outlet (Pipe Flow)

Flow recirculation characterizes the channel outlet as observed in Figure 8(c). The recirculation zones affect therefore the turbulent pipe flow in the manifold outlet. To quantify the recirculation intensity, Γ, around a fictional recirculation boundary, one can apply:

$$\Gamma = 2\pi uR \tag{7}$$

where R is the recirculation length-scale (half of the hydraulic diameter of the circulation area), roughly 9 mm, and u is the average measured fluid velocity on the fictional closed curves, just about 0.7 $m \cdot s^{-1}$. In the given conditions, the magnitude of Γ is equal to 0.04 $m^2 \cdot s^{-1}$.

With the aim of visualizing swirling flow structures at the channel outlet, bubbles have been added to the main PHE flow. Figure 9 shows a photograph of the turbulent pipe flow with air bubbles added to the main stream at the exit manifold.

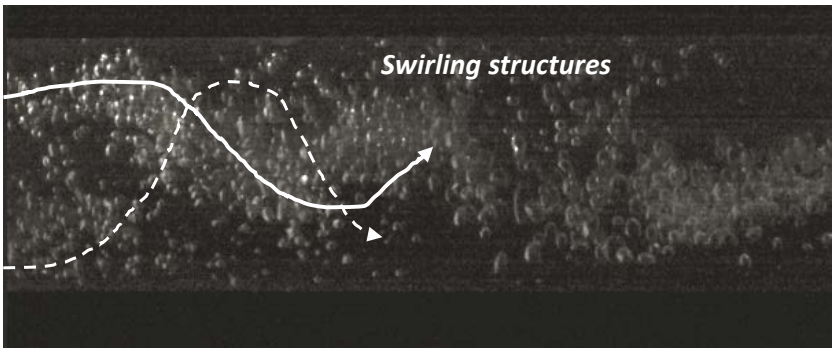

Figure 9. Visualization of swirling flow structures at the PHE channel outlet.

The necessary length to obtain a fully developed turbulent pipe flow at the channel outlet is estimated following the experimental work of Rocklage-Marliani *et al.* [35] who investigated swirling turbulent pipe flows with Laser-Doppler measurements and a swirl generator. The latters investigated pipe flow statistics in several cross-sections downstream the generator. Following Rocklage-Marliani *et al.* [35], statistics were compared with different rotation numbers (Ro) defined as:

$$Ro = \Omega D / 2v_B \tag{8}$$

where Ω is the angular velocity. A rough estimation of Ω length-scale for the present experiment is 12.7 s^{-1}. By taking v_B as 0.15 $m \cdot s^{-1}$, one estimates the rotation number as 2.4.

Escue and Cui [36] studied numerical swirling turbulent pipe flows by nu-

merical simulations and validated with the data of Rocklage-Marliani *et al.* [35]. The formers observed that swirling pipe flows with $Ro = 2$ did not achieve a fully-developed state for a distance of about 14D. In present boundary conditions, statistics of fully turbulent pipe flows are only expected for distances over 20D.

4. Conclusions

Plate Heat Exchanger channels have been assessed by experiments with three different chevron angle arrangements (30˚/30˚, 60˚/60˚ and 30˚/60˚) in turbulent flow regime. The first and second arrangements are representative of low and high pressure drop channels, respectively, while the third configuration is an attempt to achieve in-between results regarding thermal-flow performance.

For the same Reynolds number, channel pressure drop increased with increasing chevron angles owing to the increased flow disturbance in longitudinal wavy flows as compared to furrow patterns. The pressure drop in mixed channels cannot be approximated by averaging the chevron angle arrangement: it is slightly higher than the one presented for L-channels. Despite the occurrence in mixed channels of both patterns, furrow flow prevailed in the given boundary conditions. Friction factor correlations were provided for water flows with the Reynolds number ranging from 1175 to 8325.

The two-dimensional mean velocity field was obtained with the aid of Particle Tracking Velocimetry at bulk Reynolds number equal to 3450. This value was selected as to allow comparison with the velocity field of a Plate and Shell Heat Exchanger channel measured with PTV by Beckedorff *et al.* [21] with the same Reynolds number and with chevron angle arrangements of 45˚/45˚. The rectangular or circular corrugated plate geometries affect the mean velocity field. The PSHE mean velocity field is highly heterogeneous at the heat transfer area as compared to the PHE velocity field. The peak velocity magnitude in the PSHE center point is 50% higher than the PSHE bulk velocity, whereas this value is only 15% higher in the PHE center point.

The axial velocity is great in the distribution regions owing to mass conservation. The maximum average velocity reaches 2.4 times the bulk velocity at the entrance, and 2 times at the exit. The significant velocity components in these areas will play important role in the PHE dissipation process where flow deceleration and acceleration occur with high velocity components, and therefore can limit the heat exchanger thermal performance. Besides, the distribution regions are found to be potential failure locations for PHE plates and gaskets.

Fluid particle trajectories enter the PHE channel on roughly linear streamlines, while intense flow recirculation characterizes the channel outlet. The recirculation zones affect therefore the turbulent pipe flow in the manifold outlet, presenting swirling flow structures. Statistics of fully turbulent pipe flows are only expected for distances over twenty pipe diameters.

Acknowledgements

We would like to express our gratitude to FAPESC, CAPES, CNPq, and

PETROBRAS S.A. for supporting this research.

Conflicts of Interest

The authors declare no conflicts of interest regarding the publication of this paper.

References

[1] Kakaç, S., Liu, H. and Pramuanjaroenkij, A. (2012) Heat Exchangers: Selection, Rating, and Thermal Design. CRC Press.

[2] Shah, R.K. and Sekulić, D.P. (2003). Fundamentals of Heat Exchanger Design. Wiley. https://doi.org/10.1002/9780470172605

[3] Panday, N.K. and Singh, S.N. (2023) Effect of Geometrical Parameters on the Performance of Plate Heat Exchanger Using Milk-Water as Medium Fluids in the Channels. *International Journal of Thermal Sciences*, **185**, Article ID: 108022. https://doi.org/10.1016/j.ijthermalsci.2022.108022

[4] Heavner, R.L., Kumar, H. and Wanniarachchi, A.S. (1993) Performance of an Industrial Plate Heat Exchanger: Effect of Chevron Angle. AIChE Symposium Series.

[5] Talik, A.C. and Swanson, L.W. (1995) Heat Transfer and Pressure Drop Characteristics of a Plate Heat Exchanger Using a Propylene-Glycol/Water Mixture as the Working Fluid. *Proceedings of the* 30*th National Heat Transfer Conference*, Portland, 6-8 August 1995.

[6] Wang, L. and Sundén, B. (2003) Optimal Design of Plate Heat Exchangers with and without Pressure Drop Specifications. *Applied Thermal Engineering*, **23**, 295-311. https://doi.org/10.1016/s1359-4311(02)00195-3

[7] Han, D., Lee, K. and Kim, Y. (2003) Experiments on the Characteristics of Evaporation of R410A in Brazed Plate Heat Exchangers with Different Geometric Configurations. *Applied Thermal Engineering*, **23**, 1209-1225. https://doi.org/10.1016/s1359-4311(03)00061-9

[8] Khan, T.S., Khan, M.S., Chyu, M. and Ayub, Z.H. (2010) Experimental Investigation of Single Phase Convective Heat Transfer Coefficient in a Corrugated Plate Heat Exchanger for Multiple Plate Configurations. *Applied Thermal Engineering*, **30**, 1058-1065. https://doi.org/10.1016/j.applthermaleng.2010.01.021

[9] Yang, J., Jacobi, A. and Liu, W. (2017) Heat Transfer Correlations for Single-Phase Flow in Plate Heat Exchangers Based on Experimental Data. *Applied Thermal Engineering*, **113**, 1547-1557. https://doi.org/10.1016/j.applthermaleng.2016.10.147

[10] Muley, A. and Manglik, R.M. (1997) Enhanced Heat Transfer Characteristics of Single-Phase Flows in a Plate Heat Exchanger with Mixed Chevron Plates. *Journal of Enhanced Heat Transfer*, **4**, 187-201. https://doi.org/10.1615/jenhheattransf.v4.i3.30

[11] Abou Elmaaty, T.M., Kabeel, A.E. and Mahgoub, M. (2017) Corrugated Plate Heat Exchanger Review. *Renewable and Sustainable Energy Reviews*, **70**, 852-860. https://doi.org/10.1016/j.rser.2016.11.266

[12] Zhang, J., Zhu, X., Mondejar, M.E. and Haglind, F. (2019) A Review of Heat Transfer Enhancement Techniques in Plate Heat Exchangers. *Renewable and Sustainable Energy Reviews*, **101**, 305-328. https://doi.org/10.1016/j.rser.2018.11.017

[13] Arsenyeva, O., Tovazhnyanskyy, L., Kapustenko, P., Klemeš, J.J. and Varbanov, P.S. (2023) Review of Developments in Plate Heat Exchanger Heat Transfer Enhance-

ment for Single-Phase Applications in Process Industries. *Energies*, **16**, Article 4976. https://doi.org/10.3390/en16134976

[14] Focke, W.W., Zachariades, J. and Olivier, I. (1985) The Effect of the Corrugation Inclination Angle on the Thermohydraulic Performance of Plate Heat Exchangers. *International Journal of Heat and Mass Transfer*, **28**, 1469-1479. https://doi.org/10.1016/0017-9310(85)90249-2

[15] Dović, D. and Svaic, S. (2007) Influence of Chevron Plates Geometry on Performances of Plate Heat Exchangers. *Tehnički Vjesnik*, **14**, 37-45.

[16] Martin, H. (1996) A Theoretical Approach to Predict the Performance of Chevron-Type Plate Heat Exchangers. *Chemical Engineering and Processing*: *Process Intensification*, **35**, 301-310. https://doi.org/10.1016/0255-2701(95)04129-x

[17] Arsenyeva, O., Tovazhnyanskyy, L., Kapustenko, P. and Khavin, G.L. (2011) The Generalized Correlation for Friction Factor in Crisscross Flow Channels of Plate Heat Exchangers. *Chemical Engineering Transactions*, **25**, 399-404. https://doi.org/10.3303/CET1125067

[18] Arsenyeva, O.P., Tovazhnyanskyy, L.L., Kapustenko, P.O. and Demirskiy, O.V. (2012) Heat Transfer and Friction Factor in Criss-Cross Flow Channels of Plate-and-Frame Heat Exchangers. *Theoretical Foundations of Chemical Engineering*, **46**, 634-641. https://doi.org/10.1134/s0040579512060024

[19] Arsenyeva, O.P., Tovazhnyanskyy, L.L., Kapustenko, P.O. and Demirskiy, O.V. (2014) Generalised Semi-Empirical Correlation for Heat Transfer in Channels of Plate Heat Exchanger. *Applied Thermal Engineering*, **70**, 1208-1215. https://doi.org/10.1016/j.applthermaleng.2014.04.038

[20] Santos, F.J.D., Martins, G.S.M., Strobel, M., Beckedorff, L., Paiva, K.V.D. and G.Oliveira, J.L. (2024) Combined Effects of Inlet Conditions and Assembly Accuracy on Nusselt and Friction Factors of Plate Heat Exchangers. *International Journal of Thermal Sciences*, **197**, 108797. https://doi.org/10.1016/j.ijthermalsci.2023.108797

[21] Beckedorff, L., Nieuwenhuizen, R., Bolwerk, T.M.A.J., Monteiro, A.S., de Paiva, K.V., Kuerten, J.G.M., *et al.* (2019) Flow Statistics in Plate and Shell Heat Exchangers Measured with PTV. *International Journal of Heat and Fluid Flow*, **79**, Article ID: 108461. https://doi.org/10.1016/j.ijheatfluidflow.2019.108461

[22] Beckedorff, L., Martins, G.S.M., de Paiva, K.V., Oliveira, A.A.M. and Oliveira, J.L.G. (2022) Chevron Angle Effect on Plate and Shell Heat Exchangers Measured with Particle Tracking Velocimetry. *Heat Transfer Engineering*, **43**, 1885-1899. https://doi.org/10.1080/01457632.2021.2022302

[23] Laws, E.M., Lim, E.H. and Livesey, J.L. (1986) Momentum Balance in Highly Distorted Turbulent Pipe Flows. *Experiments in Fluids*, **5**, 36-42. https://doi.org/10.1007/bf00272423

[24] Sarraf, K., Launay, S. and Tadrist, L. (2015) Complex 3D-Flow Analysis and Corrugation Angle Effect in Plate Heat Exchangers. *International Journal of Thermal Sciences*, **94**, 126-138. https://doi.org/10.1016/j.ijthermalsci.2015.03.002

[25] Albrecht, H.E., Borys, M., Damaschke, N. and Tropea, C. (2003) Laser Doppler and Phase Doppler Measurement Techniques. Springer-Verlag.

[26] Oliveira, J.L.G., van der Geld, C.W.M. and Kuerten, J.G.M. (2013) Lagrangian and Eulerian Statistics of Pipe Flows Measured with 3D-PTV at Moderate and High Reynolds Numbers. *Flow, Turbulence and Combustion*, **91**, 105-137. https://doi.org/10.1007/s10494-013-9457-9

[27] Oliveira, J.L.G., van der Geld, C.W.M. and Kuerten, J.G.M. (2015) Lagrangian Ve-

locity and Acceleration Statistics of Fluid and Inertial Particles Measured in Pipe Flow with 3D Particle Tracking Velocimetry. *International Journal of Multiphase Flow*, **73**, 97-107. https://doi.org/10.1016/j.ijmultiphaseflow.2015.03.017

[28] Oliveira, J.L.G., van der Geld, C.W.M. and Kuerten, J.G.M. (2017) Concentration and Velocity Statistics of Inertial Particles in Upward and Downward Pipe Flow. *Journal of Fluid Mechanics*, **822**, 640-663. https://doi.org/10.1017/jfm.2017.289

[29] Maas, H.-G. (1996) Contributions of Digital Photogrammetry to 3-D PTV. In: Dracos, T., Eds., *Three-Dimensional Velocity and Vorticity Measuring and Image Analysis Techniques*, Springer, 191-207. https://doi.org/10.1007/978-94-015-8727-3_9

[30] Dracos, T. (1996) Particle Tracking in Three-Dimensional Space. In: Dracos, T., Eds., *Three-Dimensional Velocity and Vorticity Measuring and Image Analysis Techniques*, Springer, 209-227. https://doi.org/10.1007/978-94-015-8727-3_10

[31] Tribbe, C. and Müller-Steinhagen, H.M. (2001) Gas/liquid Flow in Plate-and-Frame Heat Exchangers—Part I: Pressure Drop Measurements. *Heat Transfer Engineering*, **22**, 5-11. https://doi.org/10.1080/01457630150215677

[32] Beckedorff, L., da Silva, R.P.P., Martins, G.S.M., de Paiva, K.V., Oliveira, J.L.G. and Oliveira, A.A.M. (2022) Flow Maldistribution and Heat Transfer Characteristics in Plate and Shell Heat Exchangers. *International Journal of Heat and Mass Transfer*, **195**, Article ID: 123182. https://doi.org/10.1016/j.ijheatmasstransfer.2022.123182

[33] Bond, M.P. (1981) Plate Heat Exchangers for Effective Heat Transfer. Institution of Chemical Engineers, 162-167.

[34] Gusew, S. and Stuke, R. (2021) Plate Heat Exchangers: Calculation of Pressure Drop for Single Phase Convection in Turbulent Flow Regime. *Heat and Mass Transfer*, **58**, 419-430. https://doi.org/10.1007/s00231-021-03099-6

[35] Rocklage-Marliani, G., Schmidts, M. and Vasanta Ram, V.I. (2003) Three-Dimensional Laser-Doppler Velocimeter Measurements in Swirling Turbulent Pipe Flow. *Flow, Turbulence and Combustion*, **70**, 43-67. https://doi.org/10.1023/b:appl.0000004913.82057.81

[36] Escue, A. and Cui, J. (2010) Comparison of Turbulence Models in Simulating Swirling Pipe Flows. *Applied Mathematical Modelling*, **34**, 2840-2849. https://doi.org/10.1016/j.apm.2009.12.018

Symbols

A_{sec}	Port area, m^2
b	Corrugation depth, m
d	Particle diameter, m
D	Pipe diameter, m
D_h	Hydraulic diameter, m
D_p	Porthole diameter, m
f	Fanning friction factor
k	Fluid thermal conductivity, $W \cdot m^{-1} \cdot K^{-1}$
l	Length-scale, m
L_h	Width between portholes, mm
L_p	Heat exchange length, mm
L_v	Length between the inlet and outlet port centers, m
L_w	Plate width, mm
$\dot{m}\_ch$	mass flow rate, $kg \cdot s^{-1}$
P	Pressure, bar
P_c	corrugation pitch, m
Pr	Prandtl number
R	recirculation boundary radius, mm
Ro	Rotation number
Re	Reynolds number
St	Stokes number
t	average channel height, m
u	average velocity on the recirculation closed curve
u_τ	wall shear velocity
v	velocity, $m \cdot s^{-1}$
x	Cartesian coordinate, m
y	Cartesian coordinate, m

Greek Symbols

β	Chevron angle, ˚
ΔP_{ch}	Channel frictional pressure drop, bar
Γ	circulation intensity, m^2/s
Ω	angular velocity, s^{-1}
μ	Dynamic viscosity, $kg \cdot m^{-1} \cdot s^{-1}$
ν	kinematic viscosity
ρ	Density, $kg \cdot m^{-3}$
τ	Time-scale
τ_w	wall shear stress
ϕ	Enlargement factor
χ	Corrugation number

Subscripts

b	bulk
ch	Channel
f	Fluid
k	Kolmogorov
p	Particle
rad	radial
w	Wall

Abbreviations

GPHE	Gasket Plate heat exchanger
PSHE	Plate and shell heat exchanger
PTV	Particle Tracking Velocimetry